Effect of Background Pressure on Ion Dynamics in an Electron Cyclotron Resonance Thruster

Benjamin N. Wachs*, and Benjamin A. Jorns†
University of Michigan, Ann Arbor, MI, 48104, USA

The effect of background pressure on the discharge properties of a 30-watt electron cyclotron resonance thruster is studied. Microwave power meters are used to determine changes in the discharge impedance while laser induced fluorescence is used to measure ion velocity distributions within the plume. Operating background pressure in the chamber is varied from 8x10^{-7} to 2x10^{-5} Torr-xenon by injecting excess xenon upstream of the thruster. It is found that microwave coupling and plasma potential within the plume are weakly dependent on chamber background pressure. Ion velocity distribution functions are found to broaden to lower energies more rapidly downstream of the thruster in the presence of high background pressure. However, it is shown that charge exchange collisions cannot fully explain this effect.

I. Nomenclature

ω_{ce}	=	electron cyclotron frequency
q	=	elementary charge
m_e	=	electron mass
B	=	magnetic flux density
ν	=	frequency
V	=	velocity
c	=	speed of light
Φ	=	plasma potential
m_{Xe}	=	xenon mass
λ_{mfp}	=	xenon mass
σ_{cex}	=	charge exchange cross section

II. Introduction

Electrodeless thruster designs offer several advantages over traditional Electric Propulsion (EP) devices such as Hall effect thrusters and gridded ion thrusters. The absence of multiple electrodes, thermionic emitters, and multiple power supplies enables simpler designs, lower thruster mass, and the use of alternative propellants [1]. A common electrodeless thruster topology utilizes a Magnetic Nozzle (MN) to convert thermal energy from the plasma source into directed thrust. Although these thrusters are simple in concept and have promising applications in small satellite propulsion, they have failed to achieve efficiencies competitive with traditional EP devices.

Typical MN thrusters have used helicon or Inductively Coupled Plasma (ICP) sources to generate and heat a plasma. These types of radiofrequency plasma generation methods have been used extensively in plasma processing due to their ability to create dense plasmas at low powers [2]. However, MN thrusters using these technologies at sub-kilowatt power levels have typically seen poor performance with thrust efficiencies under 7% and Specific Impulses (I_{sp}) around 500 seconds [3]. Recent experiments at National d'Etudes et de Recherches Aérospatiales (ONERA) using a different type of plasma heating, Electron Cyclotron Resonance (ECR), have shown greatly improved performance compared to previous MN thrusters at similar power levels. ONERA has reported efficiencies as high as 16% at an I_{sp} of 993 seconds when operating at 30 watts absorbed power [4]. ECR is a collisionless heating mechanism in which

* Ph.D. Candidate, Department of Aerospace Engineering, University of Michigan, and AIAA Student Member.
† Assistant Professor, Department of Aerospace Engineering, University of Michigan, and AIAA Senior Member

radiofrequency or microwave power is injected into a plasma at the electron cyclotron frequency. The concept of ECR driven thrusters was first proposed in the 1960's, however, microwave sources at the time were too bulky and inefficient for use on spacecraft [5]. Since then, microwave technology has seen extensive development, and recent deep space missions have used ECR as a plasma source for ion thrusters [6]. Present developments in microwave semiconductors, including Gallium Nitride transistors, have made ECR a viable candidate for low power, low mass microsatellites [7].

Although these thrusters show promising results, the physics underlying their higher performance is still largely unknown. In typical magnetic nozzles, hot electrons escape from the discharge region into a diverging magnetic field, thus creating an ambipolar potential. This potential accelerates the relatively cold ions from the thruster and produces a net thrust. The ambipolar field has been observed to extend several centimeters downstream of the thruster exit plane in ECR thrusters [8]. Because ECR is a resonant, collisionless heating mechanism, it can create higher energy electrons than ICP or helicon discharges. This effect could explain the observed performance increase, however, another possibility is that ECR simply couples a higher percentage of the injected power to the plasma compared to the previous helicon and ICP sources.

Recent experiments at ONERA have shown that thrust produced by ECR driven MN thrusters is highly dependent on vacuum chamber background pressure. Their work found that increasing chamber pressure from 1×10^{-5} to 5×10^{-5} Torr decreased thrust by 70% [9]. Further Faraday probe testing revealed the plume divergence angle significantly widened with increasing background pressure. Vialis et. al. proposed either charge exchange collisions or ambient plasma formation as possible explanations for the observed behavior. However, the physics underlying this decrease in performance is not fully understood, and furthermore, lower pressure regimes have not yet been studied. Understanding these effects is essential to developing MN thrusters and ensuring accurate ground testing results.

We investigate in this work the effect of background pressure on the ion dynamics within the magnetic nozzle region of an ECR thruster using non-invasive diagnostics. Neutral gas is pumped into the chamber upstream of the thruster to increase background pressure. The flow is simulated within the testing chamber to establish local neutral densities. Changes to the impedance of the plasma are measured using microwave power sensors, while the plume properties are studied using Laser Induced Fluorescence (LIF). The results offer a more complete description of the effects of neutral density of both the microwave-plasma coupling and the dynamics within magnetic nozzles. This paper is organized as follows: In section III, we discuss the experimental setup, in section IV we present our experimental results including neutral pressure, floating potential, microwave power, and LIF measurements. In Section V, we discuss the experimental results.

III. Experiment Setup

This experiment required both microwave and plasma diagnostics to gather a complete picture of the effects of background pressure on thruster operation. These diagnostics enabled us to distinguish between microwave coupling effects and plume collisionality effects. Below, we present the ECR thruster used for these tests and the accompanying microwave and plasma diagnostics.

A. ECR Thruster

The ECR thruster used for these experiments utilizes a coaxial design based on previous experiments performed at ONERA [4]. Gas is injected radially into the discharge chamber where a centrally mounted copper conductor excites a 2.4 GHz electromagnetic wave within the plasma. This wave couples power directly to the electrons when the input frequency is equal to the electron cyclotron frequency given by

$$\omega_{ce} = \frac{qB}{m_e} \tag{1}$$

Permanent magnets upstream of the discharge region provide a diverging magnetic field which forms both the resonance zone for ECR and the magnetic nozzle into which the plasma expands. The centerline magnetic flux density as measured from the back of the discharge region is shown in Fig. 1. The resonant magnetic field of 870 Gauss is located near the gas injection region, as shown in Fig. 1 (a). The magnetic field then forms a diverging magnetic nozzle downstream of the ECR resonance zone.

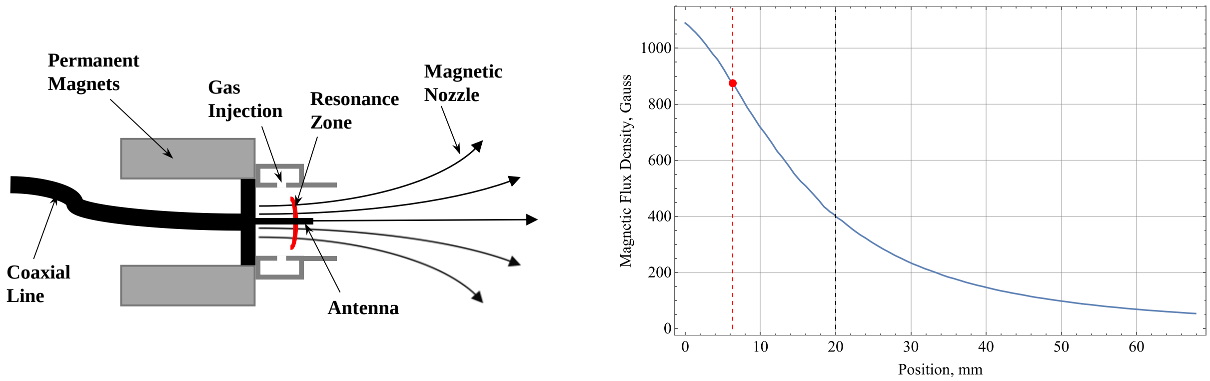

a) b)

Fig. 1 (a) Cross section of the ECR thruster and (b) centerline magnetic flux density where the red line indicates the resonant magnetic field strength, and the black line indicates thruster exit plane

The experiments presented in the paper used xenon as a propellant due to its relative ease of ionization and the availability of LIF plasma diagnostics for singly charged xenon. We used a standard flow rate of 1 SCCM for all of the experiments in the paper. The thruster is shown firing in Fig. 2. We can observe visible bright spots where the xenon is injected into the thruster.

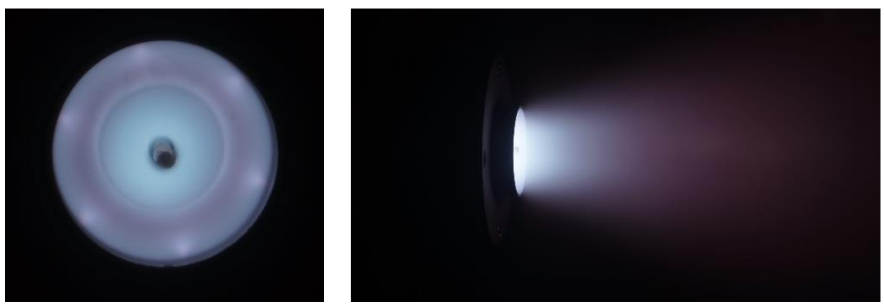

a) b)

Fig. 2 ECR thruster operating at 30 Watts and 1 SCCM xenon (a) front view, (b) side view

B. Microwave Power Injection and Measurement

The experiments in this paper were conducted in the Industrial, Scientific, and Medical (ISM) band at 2.4 GHz. The power injection scheme is shown in Fig. 3. A microwave signal generator produces a low power signal at 2.4 GHz that is then is fed into an Ampleon Solid State Power Amplifier followed by a Narda dual directional coupler. The sampled ports of the directional coupler are measured using two Mini-Circuits PWR-6GHz microwave power sensors to give forward and reflected power readings. The power sensors have an accuracy of -0.01 dBm (1 mW) at 2.4 GHz. The microwave power is then fed into the vacuum chamber using a type-N feedthrough with loss coaxial cable on either side. A DC block is used inside the vacuum chamber to float the thruster and enable measurements of the thruster's floating potential.

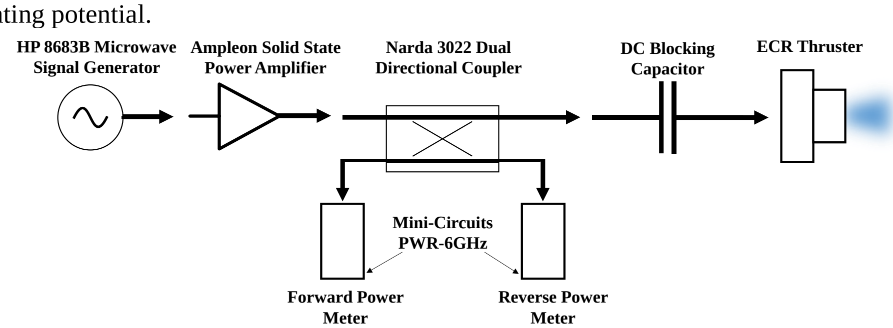

Fig. 3 Block diagram of microwave components powering the ECR thruster

C. Vacuum Facilities

The experiments were conducted in the Junior Test Facility at the University of Michigan's Plasmadynamics and Electric Propulsion Laboratory. The full setup is shown in Fig. 4. The chamber dimensions are 3 meters long by 1 meter diameter. The chamber is equipped with a Leybold Mag 2000 turbomolecular pump and a large cryogenic panel capable of pumping a combined 32,000 L/s on xenon. The chamber reached base pressures ranging from 5 x 10^{-8} Torr to 8 x 10^{-7} throughout the experimental campaign. Operating pressures ranged between 7 x 10^{-7} Torr and 5 x 10^{-5} Torr for the conditions tested in the paper.

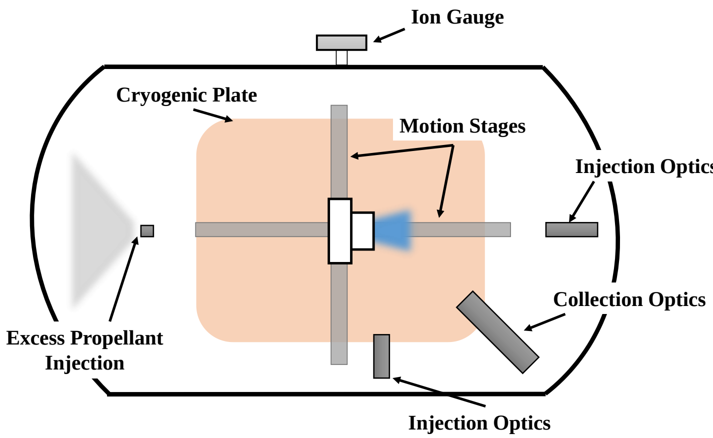

Fig. 4 Junior test facility setup

D. Diagnostics

We measured neutral densities using a Varian 563 Ion Gauge mounted at the midplane of the chamber wall, while plasma properties were measured using LIF diagnostics based on techniques used in previous experiments at PEPL [8] [9]. We determined changes in discharge impedance using the microwave power meters described above.

We employed a time averaged LIF diagnostic scheme which used a tunable laser to excite an 834.953 nm (vacuum) metastable state in Xe II, which fluoresces at 542.066 nm (vacuum). The input wavelength is swept such that the doppler shifted frequency seen by the ion matches the excitation frequency of the metastable state. The doppler shifted frequency is given by

$$\nu = \left(1 + \frac{V}{c}\right)\nu_0 \tag{2}$$

where V is the ion velocity, ν is the observed frequency, ν_0 is the frequency in a stationary frame, and c is the speed of light.

This setup has been used in several previous experiments at PEPL and is briefly described here. A New Focus Velocity TLB-6716 diode laser with an output wavelength range of 830-853 nm is fed into a New Focus TA-7616 Tapered amplifier with a maximum output power of 1 W. The laser is swept from approximately 834.94 to 835.0 nm to excite ions travelling between -5,000 and 16,000 m/s. The light is distributed to a HighFinesse WS-7 wave meter and three optical choppers with chopping frequencies from 2000 to 3000 Hz. Two of the chopped signals are fed into the chamber while the third is coupled to a Hamamatsu L2783-42 XeNe-Mo optogalvanic cell used to calibrate the measurements. The injection optics are placed orthogonally to measure axial and radial ion velocity distribution functions, as shown in Fig. 4.

The collected light from the chamber and optogalvanic cell is fed into a SPEX-500M spectrometer, which filters light outside of a 1 nm band centered around 542 nm. This signal is coupled to a Hamamatsu R928 photomultiplier tube to amplify the signal and then fed to three Stanford Research Systems SR810 lock-in amplifiers to measure the collected light intensity at the specified chopping frequencies. The data from the lock-in amplifiers and the wave meter are then compared to produce velocity distribution functions. Time constants for the lock-in amplifiers varied from 100ms close to the thruster exit plane, to 3 seconds at 97mm downstream of the thruster.

Because of the relatively high magnetic field strength close to the thruster exit plane, the effect of Zeeman splitting must be considered. Using the effective shift in frequency due to Zeeman splitting given by Huang [12]:

$$\Delta f = 2.7273B \text{ (MHz/Gauss)} \tag{3}$$

where B is the magnetic field strength, we can calculate that at the exit plane, where the magnetic field strength is 400G, the shift in wavelength is 1.09GHz. This corresponds to a change in observed velocity of 910 m/s. Because the velocity distribution at the exit plane spans over 5000 m/s and the magnetic field strength decreases exponentially downstream of the thruster, the effect of Zeeman splitting is ignored for the analysis presented in this paper.

E. Methodology

We operated the ECR thruster at a constant forward power of 30 watts and xenon flow rate of 1 SCCM for each of the pressure conditions studies. Reflected power varied from tens of milliwatts to just over 1 watt throughout the experiments, and therefore the absorbed power varied slightly as background pressure changed. However, we found that over all of the conditions tested, the absorbed power changed by less than 1%. We employed water cooling at the thruster to ensure constant magnet temperature, thus avoiding thermal demagnetization effects.

We adjusted background pressure using a technique similar to that performed at ONERA [9]. Excess xenon was pumped into the vacuum chamber through a gas feed line pointed towards the back wall of the vacuum chamber, 0.75 meters upstream of the thruster, as shown in Fig. 4. Flowrates for the background xenon were varied between 0 and 50 SCCM, however, LIF data were only taken at the 0, 20, and 40 SCCM conditions. We collected data with the thruster placed on a motion stage while the optics and pressure gauge were held in a fixed position.

We measured ion VDF data in 5 mm increments along a line extending from 2 mm within the thruster discharge region to 97 mm downstream of the thruster exit plane. The LIF interrogation volume was 1 mm^3 with a 2 mm uncertainty in position. We chose to offset the measurements 5 mm from thruster centerline as the plasma density was higher than on centerline, and we were able to capture bulk radial expansion effects that could not be observed directly on centerline.

IV. Results

A. Pressure Measurements

Pressure measurements were recorded with the thruster firing at 1 SCCM with excess flow rates ranging from 0 SCCM to 40 SCCM. No change in pressure reading was observed when the thruster was firing versus when purely cold gas was flowed through the thruster. Fig. 9 shows the measured points plotted on a linear scale. The data showed a relatively constant pumping speed of around 30,000 L/s. These measurements are in agreement with the theoretical pumping capacity of the Junior test facility.

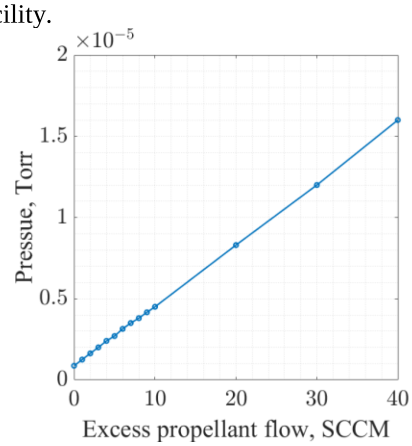

Fig. 9 Chamber pressure (Torr) vs excess propellant flow rate for the 1 SCCM thruster operating condition

As pressure was increased in the chamber, the plasma discharge was observed to change color from a whitish blue plume to a pinker hue. Additional plasma was observed downstream of the thruster as pressure was increased. The thruster is shown firing in low and high pressure configurations in Fig. 10. Although not definitive, these visual changes indicate that a higher population of excited neutrals exists within the plume during high pressure operation, indicative of higher electron-neutral collisions.

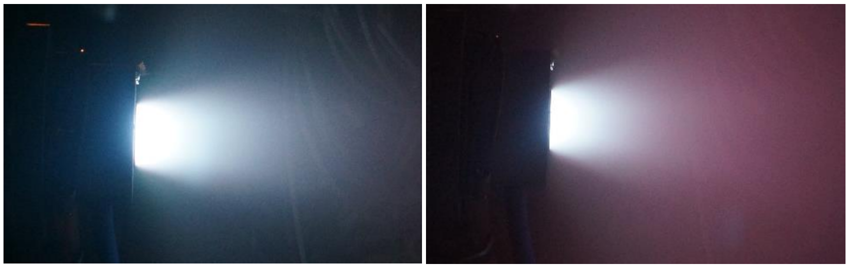

a) b)

Fig. 10 Thruster firing at 30 W, 1 SCCM in (a) 1.25 x 10^{-6} Torr and (b) 1.6 x 10^{-5} Torr background pressures

B. Floating Potential

We measured the thruster's floating potential with respect to chamber ground by attaching a lead to the thruster body. It was observed that the potential was highly dependent on the background pressure within the chamber. As shown in Fig. 11, the floating potential decreases exponentially as background pressure increases from 8 x 10^{-7} to 2 x 10^{-5} Torr. It is unclear if this decrease is indicative of thruster performance, but the data demonstrates the system's sensitivity to small changes in background pressure.

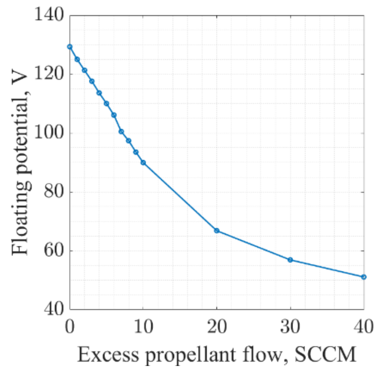

Fig. 11 Floating potential measured for excess flow conditions from 0 SCCM to 40 SCCM

C. Microwave Diagnostics

The power reflection coefficient for each operating condition was calculated by dividing the reverse power by the forward power measured by the microwave power meters attached the directional coupler. The reflection coefficient was observed to vary by around 20% for the background pressures tested, as shown in Fig. 12 (a), while total absorbed power varied by less than 1%, shown in Fig. 12 (b).

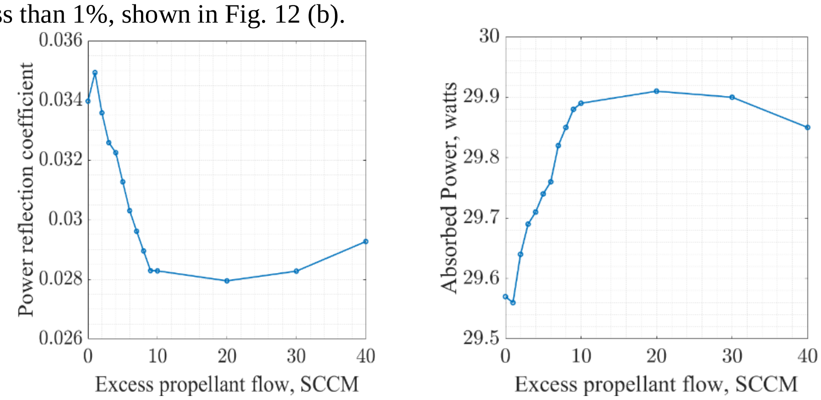

a) b)

Fig. 12 Reflection coefficient measured at the directional coupler versus excess flow

These results give a somewhat linear dependence of reflected power on the propellant density within the thruster, which we show Section V varies by about 15% over the flow conditions tested. These data seem to indicate that the plasma impedance properties were largely unchanged throughout the tests, meaning that the decrease in performance was likely not due to fundamental changes in microwave coupling. However, it is not possible to definitively say where microwave power is coupling without more advanced diagnostics.

D. LIF Data

The axial and radial VDF data are shown in Fig. 13 and Fig. 14. The VDF at each axial location is largely unchanged for each of the three background pressures tested. Higher pressure tests yielded much lower signal to noise ratios than the nominal operating condition, making direct comparisons difficult. The VDFs reveal an accelerated and a stationary ion populations present in the plasma. The most probable velocity of the high energy population is starred for the axial plots. It is worth noting that the stationary ion population seen in these VDFs disappears when measurements are taken further off centerline. It is possible that this phenomenon is caused by an annular discharge being formed around the microwave antenna within the discharge region.

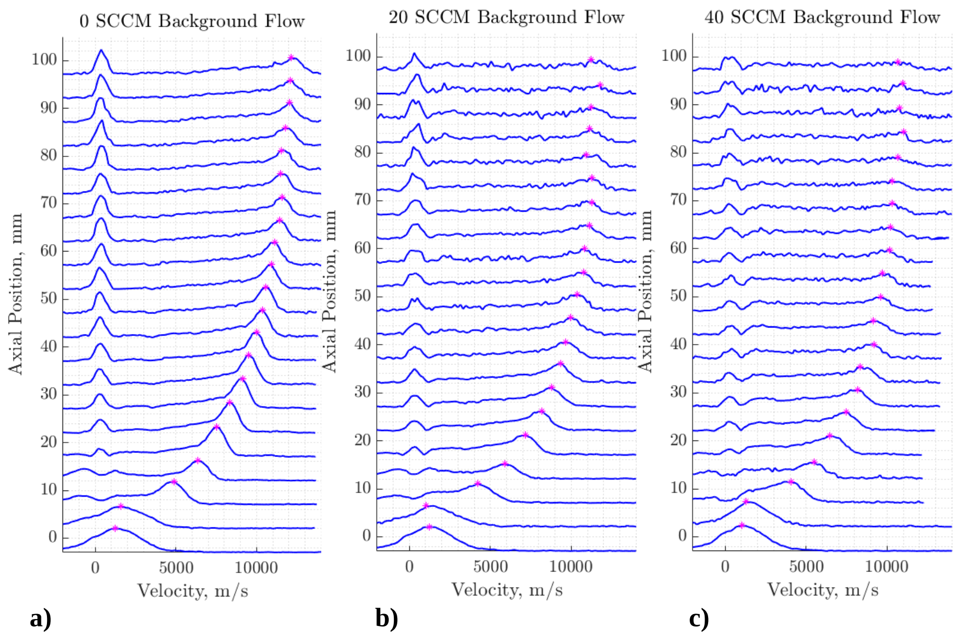

Fig. 13, Axial VDFs for (a) 0 SCCM excess flow, (b) 20 SCCM excess flow, and (c) 40 SCCM excess flow. The starred points give the location of the most probable velocity of the high energy distribution

Overlaying the axial and radial VDFs close to the thruster exit plane in Fig. 15, we can see that the VDF broadens towards lower energies more rapidly for higher background pressure operating points. These data are consistent with higher collision rates with cold background neutrals within the plume. These collisions could explain the decrease in performance seen at high pressures, as high energy electrons and ions lose their energy to cold neutrals, and will be discussed further in the following section.

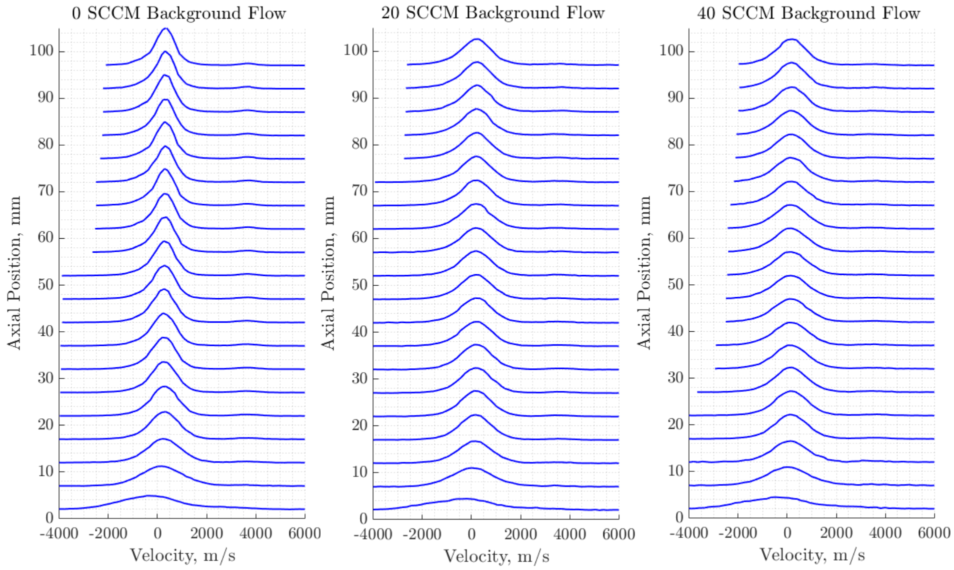

a) **b)** **c)**

Fig. 14 Radial VDFs for (a) 0 SCCM excess flow, (b) 20 SCCM excess flow, and (c) 40 SCCM excess flow

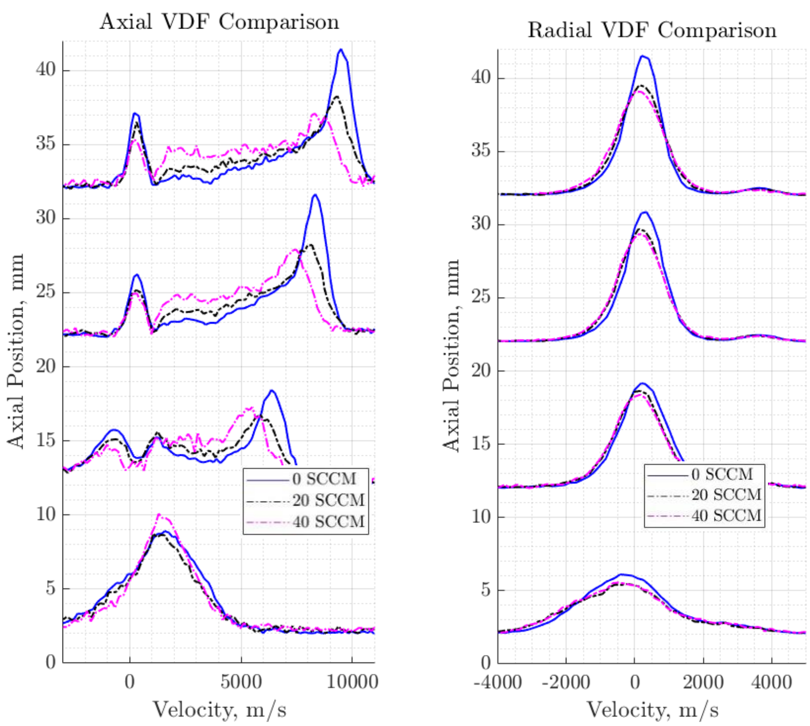

a) **b)**

Fig. 15 (a) Axial VDF comparisons and (b) radial VDF comparisons close the thruster exit plane

We plot the most probably velocity of the high energy population for all three flow conditions in Fig. 16 (a). Neglecting ionization and ion pressure effects, and setting the potential at the thruster exit plane to 0 V, we obtain the plasma potential at the measured axial positions using:

$$\Phi = -\frac{m_{Xe}V_z^2}{2q_e} \tag{4}$$

where V_z is the most probable velocity of the high energy population, m_{xe} is the xenon atomic mass, and q_e is the elementary charge. We plot the calculated plasma potential for all three flow conditions in Fig. 16 (b).

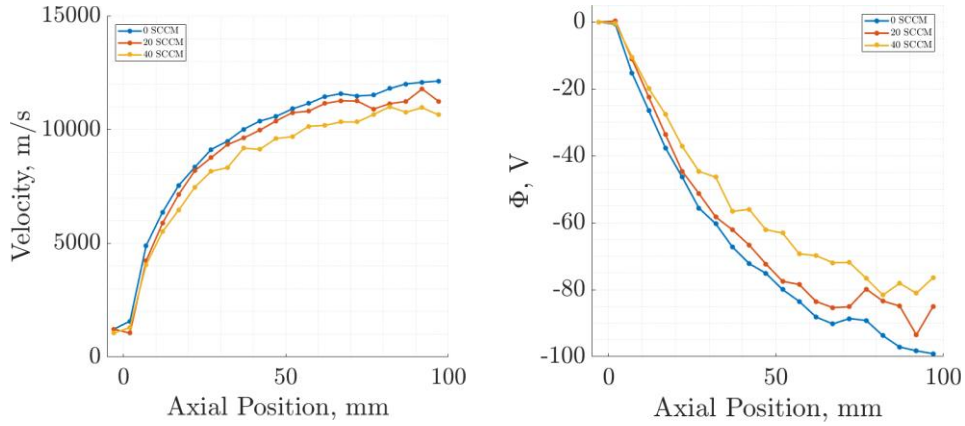

a) b)

Fig. 16 (a) Most probable axial velocity for the high energy population, (b) calculated plasma potential

From these plots, we can observe that the potential structure is qualitatively similar for all three conditions. Overall potential drops vary by around 20% which could explain some of the decrease in performance seen in higher pressure operation but cannot explain the full 70% reduction in thrust seen in by Vialis et al. [9]. However, because this thruster has not yet been tested on a thrust stand, we cannot know with any certainty exactly how much performance decrease to expect. It should also be noted that the potential drops calculated from the LIF data also cannot completely explain the change in thruster floating potential observed in Fig. 11.

V. Discussion

In order to further elucidate the effects of neutral gas density, we simulated neutral density profiles for three test cases using the COMSOL Multiphysics Free Molecular Flow package. The vacuum chamber and accompanying pumps were represented in a simplified axisymmetric geometry, as shown in Fig. 17 (a). The thruster was simulated as a solid body, and the antenna geometry was ignored. The mesh used for the simulations and a closeup of the mesh used for the discharge region of the thruster are shown in Fig. 17 (a) and (b). The thruster was simulated using the 1 SCCM flowrate used throughout the experimental campaign. The background pressure was simulated for the 0, 20, and 40 SCCM excess flow rates tested during the LIF experiments. Plasma effects were not included in the simulations.

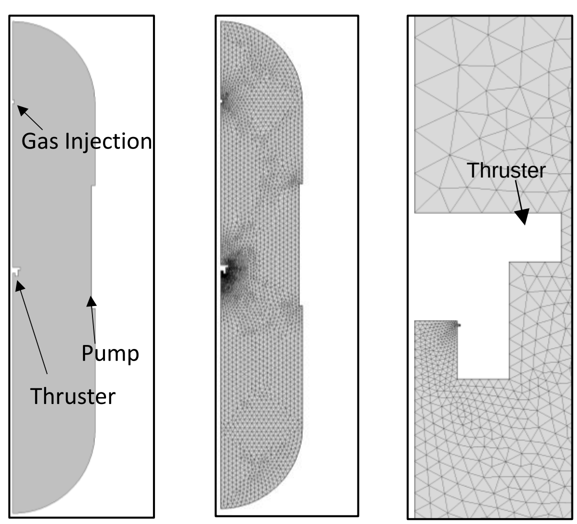

a) b) c)

Fig. 17 Axisymmetric simulation: (a) geometry, (b) mesh, and (c) a closeup of the discharge region mesh

A. Simulation Results

The simulated number density for the three cases is shown on a log plot in Fig. 18. Neutral density along the boundaries of the vacuum chamber is simulated to vary from 10^{16} m^{-3} at no excess flow to 7 x 10^{17} m^{-3} for the 40 SCCM case. Assuming the neutrals are at room temperature, these simulations yield background pressures ranging from 3 x 10^{-7} in the 0 SCCM case to 2 x 10^{-5} Torr in the 40 SCCM case. These pressures are consistent with the values measured during the experimental campaign, as described in the previous section.

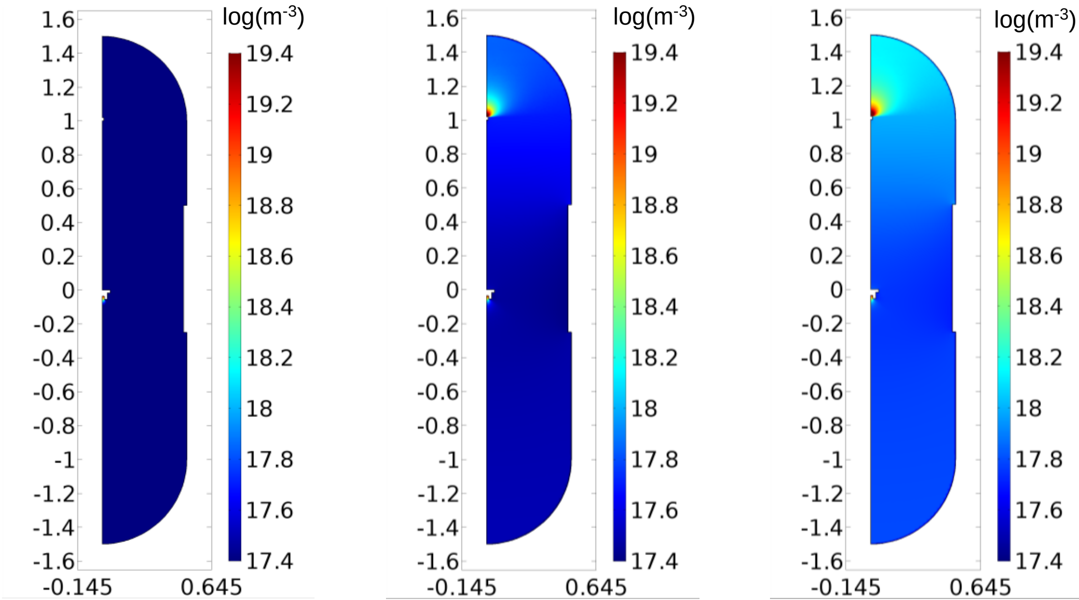

a) b) c)

Fig. 18 Log plot of neutral density, log(m^{-3}), for additional xenon flow rates of (a) 0 SCCM, (b) 20 SCCM, and (c) 40 SCCM

Looking more closely at the thruster's discharge region in Fig. 19, we observe that neutral densities within the thruster vary by only a few percent, even as the background density is increased by over an order of magnitude. Fig. 20 (a) and (b) show the density plotted along the centerline and thruster face for the three flow conditions. Fig. 20 (c) shows the density at the varying background pressures at the thruster exit plane, 5 mm off centerline where the LIF measurements were taken.

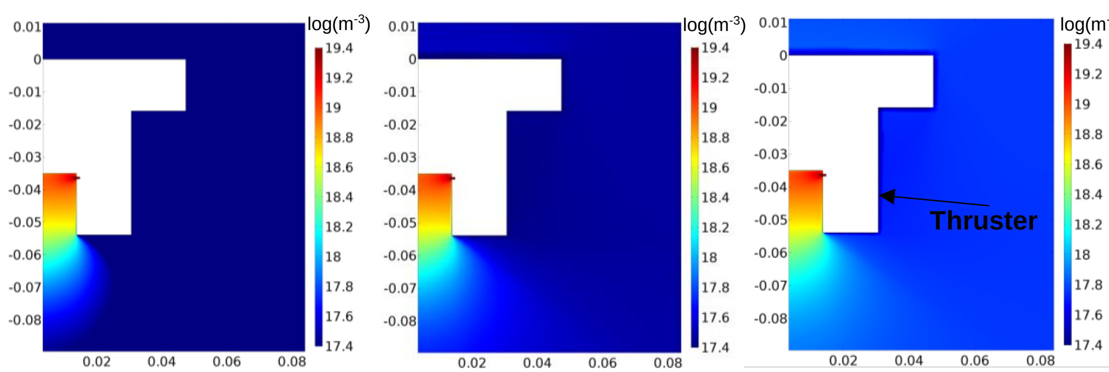

a) b) c)

Fig. 19 Log plot of neutral density near the thruster, log(m^{-3}), for additional xenon flow rates of (a) 0 SCCM, (b) 20 SCCM, and (c) 40 SCCM

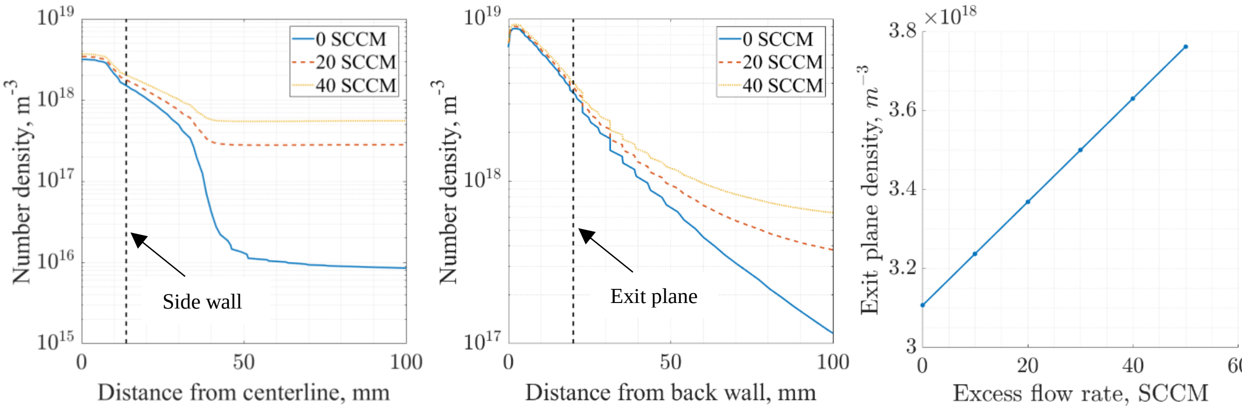

Fig. 20 Number density vs position for (a) radial distance from centerline along thruster exit plane, and (b) axial distance from the back wall along thruster centerline. (c) Exit plane density at 5 mm from centerline

From these plots, we observe that the pressure within the thruster changes by less than 15% while the pressure downstream varies by almost an order of magnitude for the positions measured during the LIF testing. These data, along with the broadening of the VDFs observed at high pressures in the preceding section seem to indicate that charge exchange collisions could play an import role in these experiments. However, as we show in the following section, this may not be the case.

B. Charge Exchange Mean Free Path

Based on the simulated pressure results, we can calculate a mean free path for charge exchange collisions given by

$$\lambda_{mfp} = \frac{1}{n\sigma_{cex}} \tag{5}$$

where σ_{cex} is the charge exchange cross section for xenon, and n is the number density. We can approximate the charge exchange cross section as a constant 10^{-18} m^2 for the ion energies seen in these experiments [13]. The results of these calculations are plotted in Fig. 21.

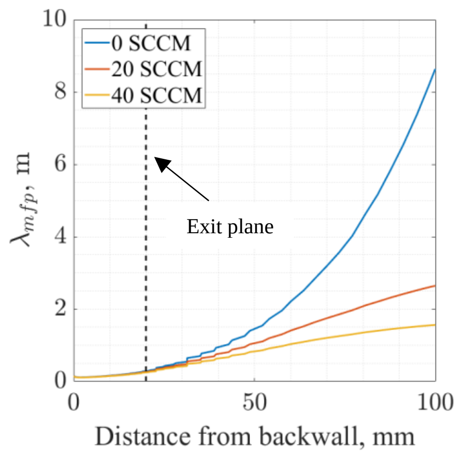

Fig. 21 Mean free path for charge exchange collisions at the three flow conditions tested

We can observe that the charge exchange mean free path is around 0.25 meters at the thruster exit plane for the three flow conditions tested. The mean free path continues to increase as we look further downstream of the thruster exit plane. These calculated mean free paths are much greater than the distance over which the VDF broadening can be observed in the LIF data, and therefore can only partially explain the lowering of ion energies at increasing background pressures.

VI.Conclusions

Increasing background pressure during testing of an ECR magnetic nozzle thruster was shown to change both the plume dynamics and the microwave power coupling characteristics. It was shown that plasma potentials decreased by 20% as background pressure was raised from 7 x 10^{-7} to 5 x 10^{-5} Torr-xenon. Ion VDFs within the plume spread to lower energies downstream of the thruster as background pressure was increased. However, this effect could not be fully captured by charge exchange collisions in the plume. The absorbed microwave power was shown to be weakly affected by changes in background pressure, but further investigation is required to determine if microwave power coupling regions change. It can be concluded from this work that a lower limit on pressure has not yet been established. Given that pressures in low Earth orbit are less than 10^{-10} Torr, it is worth continuing to investigate these phenomena at even lower pressures.

VII. Acknowledgments

This work was supported by NASA Space Technology Research Fellowship grant 80NSSC17K0157. Thank you to Eric Viges for the extensive help getting the vacuum systems running, and to the fellow members of the Plasmadynamics and Electric Propulsion Laboratory for their support with the LIF diagnostics and many insightful conversations.

VIII. References

[1] S. N. Bathgate, M. M. M. Bilek, and D. R. Mckenzie, “Electrodeless plasma thrusters for spacecraft: a review,” *Plasma Sci. Technol.*, vol. 19, no. 8, p. 083001, Aug. 2017.

[2] F. F. Chen, “Helicon discharges and sources: a review,” *Plasma Sources Sci. Technol.*, vol. 24, no. 1, p. 014001, Jan. 2015.

[3] J. Navarro-Cavalle, E. Ahedo, M. Merino, V. Gomez, and M. Ruiz, “Helicon Plasma Thrusters: prototypes and advances on modeling,” presented at the The 33rd International Electric Propulsion Conference, The George Washington University, 2013.

[4] F. Cannat, T. Lafleur, J. Jarrige, P. Chabert, P.-Q. Elias, and D. Packan, “Optimization of a coaxial electron cyclotron resonance plasma thruster with an analytical model,” *Phys. Plasmas*, vol. 22, no. 5, p. 053503, May 2015.

[5] R. G. Jahn, *Physics of electric propulsion*, Dover ed., Unabridged republication. Mineola, NY: Dover Publ, 2006.

[6] H. Kuninaka, K. Nishiyama, I. Funaki, T. Yamada, Y. Shimizu, and J. Kawaguchi, “Powered Flight of Electron Cyclotron Resonance Ion Engines on Hayabusa Explorer,” *J. Propuls. Power*, vol. 23, no. 3, pp. 544–551, May 2007.

[7] B. Green, K. Moore, D. Hill, M. C. Debaca, and J. Schultz, “Gallium Nitride RF Technology Advances and Applications,” *Edicon-China*, 2014.

[8] J. Jarrige, P.-Q. Elias, and D. Packan, “Investigation on the ion velocity distribution in the magnetic nozzle of an ECR plasma thruster using LIF measurements,” presented at the 35th International Electric Propulsion Conference, Atlanta, GA.

[9] T. Vialis, J. Jarrige, and D. Packan, “Geometry optimization and effect of gas propellant in an electron cyclotron resonance plasma thruster,” presented at the 35th International Electric Propulsion Conference, Atlanta, GA, 2017.

[10] T. Collard, M. Byrne, S. Hepner, C. J. Durot, and B. Jorns, “Investigation of Detachment in a Miniature Magnetic Nozzle Source,” presented at the 35th International Electric Propulsion Conference, Atlanta, GA, 2017.

[11] C. J. Durot, B. A. Jorns, E. T. Dale, and A. D. Gallimore, “Laser-Induced Fluorescence Measurement of the Anomalous Collision Frequency in a 9-kW Magnetically-Shielded Hall Thruster,” presented at the 35th International Electric Propulsion Conference, Atlanta, GA, 2017.

[12] W. Huang, “Study of Hall Thruster Discharge Channel Wall Erosion via Optical Diagnostics,” University of Michigan, 2011.

[13] J. S. Miller, S. H. Pullins, D. J. Levandier, Y. Chiu, and R. A. Dressler, “Xenon charge exchange cross sections for electrostatic thruster models,” *J. Appl. Phys.*, vol. 91, no. 3, pp. 984–991, Feb. 2002.